PNAS RESEARCH ARTICLE | CELL BIOLOGY

Iron regulatory protein 2 contributes to antimicrobial immunity by preserving lysosomal function in macrophages

Chen Cheng[a], Zhiyao Xing[a], Wenxin Zhang[a], Lei Zheng[b], Hongting Zhao[a], Xiao Zhang[a], Yibing Ding[a], Tong Qiao[b], Yi Li[c], Esther G. Meyron-Holtz[d], Fanis Missirlis[e], Zhiwen Fan[f,1], and Kuanyu Li[a,1]

Affiliations are included on p. 12.

Edited by Ana Maria Cuervo, Albert Einstein College of Medicine, Bronx, NY; received December 13, 2023; accepted June 4, 2024

Colorectal cancer and Crohn's disease patients develop pyogenic liver abscesses due to failures of immune cells to fight off bacterial infections. Here, we show that mice lacking iron regulatory protein 2 (*Irp2*), globally (*Irp2*$^{-/-}$) or myeloid cell lineage (*Lysozyme 2 promoter-driven, LysM*)-specifically (*Irp2*$^{\Delta LysM}$), are highly susceptible to liver abscesses when the intestinal tissue was injured with dextran sodium sulfate treatment. Further studies demonstrated that *Irp2* is required for lysosomal acidification and biogenesis, both of which are crucial for bacterial clearance. In *Irp2*-deficient liver tissue or macrophages, the nuclear location of transcription factor EB (Tfeb) was remarkably reduced, leading to the downregulation of Tfeb target genes that encode critical components for lysosomal biogenesis. Tfeb mislocalization was reversed by hypoxia-inducible factor 2 inhibitor PT2385 and, independently, through inhibition of lactic acid production. These experimental findings were confirmed clinically in patients with Crohn's disease and through bioinformatic searches in databases from Crohn's disease or ulcerative colitis biopsies showing loss of IRP2 and transcription factor EB (TFEB)-dependent lysosomal gene expression. Overall, our study highlights a mechanism whereby Irp2 supports nuclear translocation of Tfeb and lysosomal function, preserving macrophage antimicrobial activity and protecting the liver against invading bacteria during intestinal inflammation.

IRP2 | lysosomal function | TFEB localization | lactic acid | HIF2

Significance

Iron regulatory protein 2 (Irp2), an Irp in cytoplasm, is mainly responsible for cellular iron homeostasis. In this study, we show that Irp2 affects lysosome biosynthesis and acidification through hypoxia-inducible factor 2 and its target gene lactate dehydrogenase A in macrophages. Irp2 is essential for the macrophage's immune function in clearing pathogens against infection. Lactic acid production or hypoxia-inducible factor 2 inhibitors are potential therapeutical treatments for inflammatory bowel disease with or without pyogenic liver abscesses.

Pyogenic liver abscess (PLA) is sign of severe liver disease that results from the invasion of suppurative bacteria into the liver parenchyma and source of significant global public health concerns (1). PLA occurs under various conditions, such as biliary tract disease, colitis, pancreatitis, intravenous drug use, and trauma (2). The incidence of PLA ranges from 1.1 to 18 per 100,000 person-years, and the fatality rate can reach up to 30% due to the associated severe complications in patients (3, 4). Patients with inflammatory bowel disease (IBD) have a higher risk of PLA incidence (5), estimated at approximately 7 per 10,000 patients with IBD (6, 7). One suggestion why patients with Crohn's disease or ulcerative colitis are at high-risk of developing this complication is that gut barrier disruption in colitis enhances microbe infiltration into the submucosae, which increases the probability that gut-derived bacteria are translocated from the gut to the liver (7–9). In some cases, the bacterial origin of the liver abscess from gut bacteria was confirmed (6, 10, 11). Therefore, proper homeostasis of the gut barrier is crucial to maintaining a healthy liver.

Macrophages are critical in maintaining the homeostasis of the gut–liver axis by preventing bacterial translocation. Macrophages reside along the entire length of the gastrointestinal tract and throughout all layers of the gut wall, strategically positioned to engulf and destroy any bacteria penetrating the epithelial barrier, preventing bacteria translocation to the portal vein (reviewed in ref. 12). Hepatic inflammation in patients with cirrhosis affects macrophage function, leading to inadequate bacterial clearance and making patients particularly prone to developing organ failure due to infection (13). Impaired clearance by intestinal macrophages also triggers a compensatory adaptive immune response, resulting in chronic inflammation that worsens Crohn's disease (14). Recently, Galy and collaborators demonstrated that iron regulatory proteins 1 and 2 (Irp1/2) participate in the immune function of macrophages, presenting evidence that the *Irp1/2* double-knockout (KO) significantly reduced its survival rate when challenged by intraperitoneal injection of *Salmonella sp.* (15). The authors described that the *Irp1/2* KO animals retained immature neutrophils with abnormally high glycolytic activity, suggesting that neutropenia was a key underlying mechanism (16).

IRP1 and IRP2 have mostly redundant functions in regulating cellular iron homeostasis through their RNA-binding activity to iron-responsive elements (IRE) that are conserved primary mRNA sequences folding into secondary stem-loop structures (17). Under low iron conditions, IRP1 and IRP2 inhibit the translation of transcripts involved in iron

Author contributions: C.C., Z.F., and K.L. designed research; C.C., Z.X., W.Z., L.Z., H.Z., and X.Z. performed research; C.C., Y.D., T.Q., Y.L., E.G.M.-H., and F.M. analyzed data; Y.L. and Z.F. provided patient samples; Z.F. and K.L. provided funding support; and C.C., E.G.M.-H., F.M. and K.L. wrote the paper.

The authors declare no competing interest.

This article is a PNAS Direct Submission.

[1]To whom correspondence may be addressed. Email: fanzhiwenfff@126.com or likuanyu@nju.edu.cn.

This article contains supporting information online at https://www.pnas.org/lookup/suppl/doi:10.1073/pnas.2321929121/-/DCSupplemental.

Published July 24, 2024.

storage and export of efflux by binding to IRE in the 5′-Untranslated Region (UTR) of respective mRNAs such as ferritin H&L (FTH and FTL) and ferroportin. Conversely, IRPs stabilize mRNAs to promote the expression of genes responsible for iron import and utilization by binding to IREs in the 3′-UTR of mRNA, such as divalent metal transporter 1 and transferrin receptor 1. The main difference between IRP1 and IRP2 is seen under high iron conditions, where IRP1 gains cis-aconitase activity and loses IRE binding activity by assembling an iron-sulfur cluster (4Fe-4S), whereas IRP2 undergoes iron-dependent degradation. Deleting either *Irp1* or *Irp2* in mice does not affect the survival of these mice, but the preclinical manifestations are different (reviewed in ref. 18). Overall, Irp2 dominates the regulation of iron homeostasis in vivo since *Irp1* ablation mis-regulates iron metabolism only in the kidney and brown fat, whereas *Irp2* ablation mis-regulates the expression of target proteins in all tissues (19).

Our previous studies have shown that *Irp2* ablation leads to an energy-metabolism switch from oxidative phosphorylation to aerobic glycolysis in mouse embryonic fibroblasts (20), suggesting a potential role of *Irp2* ablation in promoting tumor growth. To establish a model of colon cancer, we exposed both wild type (WT) and $Irp2^{-/-}$ mice to azoxymethane/dextran sodium sulfate (DSS) treatment. To our surprise, we found that some $Irp2^{-/-}$ mice died in the second week of treatment without the occurrence of colon cancer. The autopsy revealed that DSS-induced liver injury and abscesses are the likely cause of death. Further studies elucidated the essentiality of *Irp2* in macrophage-lysosomal biogenesis and function, particularly in clearing pathogens in mice and human subjects.

Results

Liver Abscesses Occur Following DSS Treatment in $Irp2^{-/-}$ and $Irp2^{\Delta LysM}$ Mice. WT and *Irp2* KO mice were exposed to 2.5% DSS in their drinking water for 7 d, followed by 3 d of regular water and then an additional 7 d of 2.5% DSS as shown in Fig. 1*A*. This exposure to DSS is well tolerated by WT but the mortality rate of $Irp2^{-/-}$ mice was 33% in the second week and reached 45% at the experimental endpoint (n = 30) (Fig. 1*B*). $Irp2^{-/-}$ mice also experienced significant weight loss (greater than 20%) at the endpoint of DSS treatment (Fig. 1*C*). To investigate the cause of these phenotypes, we conducted routine blood tests, biochemical examinations, and autopsy. The results showed a significantly increased number of inflammatory white blood cells (*SI Appendix*, Fig. S1) and increased alanine transaminase and aspartate aminotransferase activities (Fig. 1*D*), the former finding indicating high inflammation and the latter liver dysfunction. Upon gross examination, we identified many white or yellowish spots in the $Irp2^{-/-}$ liver (Fig. 1*E*). Hematoxylin and Eosin (H&E) staining confirmed liver damage and massive infiltration of proinflammatory cells, a typical liver abscess feature, found exclusively in $Irp2^{-/-}$ mice (Fig. 1*F*). To determine the presence of infection, gram-positive staining and blood plate cultures were carried out. These assays confirmed the presence of gram-positive bacteria (Fig. 1*G*) and significant bacterial loads (Fig. 1 *H* and *I*) in the livers of $Irp2^{-/-}$mice after DSS treatment. As DSS often induces intestinal barrier damage (21), we hypothesized that the liver abscess could be due to bacterial translocation from the intestine. To verify this hypothesis, we also examined peripheral and portal vein blood with blood plate assays. The results showed large quantities of bacteria in the $Irp2^{-/-}$ portal veins after DSS treatment but barely any in peripheral blood (Fig. 1 *H* and *I*). In combination, these findings suggested that intestinal bacteria enter through the damaged intestinal barrier into the portal veins and then colonize the livers of $Irp2^{-/-}$ mice.

We then investigated whether intestinal macrophage function was affected by *Irp2* deficiency, as these cells are the front line of defense against bacterial invasion. The intestinal macrophages are commonly considered continuous replenishers derived from myeloid monocytes circulating in the bloodstream due to constant exposure to commensal microbes and low-grade inflammation (22). To generate *Irp2*-ablation mice in myeloid cell lineage, we purchased $Irp2^{flox/flox}$ mice from Cyagen Biosciences Inc. (Suzhou, China) and crossed them with the same genetic background (C57BL6J) $LysM^{cre}$ mice (Fig. 2*A*). We first confirmed the KO efficiency by showing loss of Irp2 in isolated bone marrow–derived macrophages (BMDM) (Fig. 2*B*). The resulting $Irp2^{\Delta LysM}$ mice were subjected to the same DSS treatment as $Irp2^{-/-}$ mice mentioned in Fig. 1. Similar results were obtained to those of global *Irp2*-ablation mice regarding body weight and mortality rates (Fig. 2 *C* and *D*). Additionally, only $Irp2^{\Delta LysM}$ mice had liver abscesses (Fig. 2*E*). These findings suggest that myeloid cell *Irp2* deficiency can increase the risk of DSS-induced liver abscesses. The presence of bacteria in the liver was confirmed by H&E staining, gram-positive staining, and blood plate assays, which showed that the bacteria originated from the barrier-injured intestine and colonized in the liver of $Irp2^{\Delta LysM}$ after DSS treatment (Fig. 2 *F*–*I*). The results indicate the critical role of Irp2 in the myeloid cell lineage against bacterial infection in mice.

Decreased Bacterial Clearance in $Irp2^{-/-}$ Macrophages after Treatment with *Escherichia coli*. Macrophages eliminate pathogens through phagocytosis, phagosome maturation, and pathogen clearance (23). To determine whether *Irp2* depletion affected the phagocytic or clearance capacity of macrophages, the isolated BMDM or peritoneal macrophages were treated with Dextran-Fluorescein Isothiocyanate (FITC) or enhanced green fluorescent protein (eGFP)- or mCherry-expressing *E. coli* for 15 min to evaluate phagocytosis or for 1 h to assess pathogen clearance competence. There was no significant difference in fluorescence intensity and the number of bacterial colonies after 15 min of incubation (*SI Appendix*, Fig. S2 *A*–*C*), suggesting a similar phagocytosis capacity of WT and $Irp2^{-/-}$ mutant macrophages. However, after 1 h of incubation, the number of bacteria and the fluorescence intensities of mCherry- and eGFP-*E. coli* were substantially increased in $Irp2^{-/-}$ macrophages (Fig. 3 *A* and *B* and *SI Appendix*, Fig. S2*D*), suggesting a critical role of Irp2 in pathogen clearance. To further confirm the results, we incubated BMDM and peritoneal macrophages with *E. coli* for 15 min, removed the extracellular bacteria, and allowed an additional incubation for 60 min. The macrophages were then lysed, and the bacteria were counted on Luria-Bertani (LB)-agar plates. A higher number of bacterial colonies were derived from $Irp2^{-/-}$ BMDM (371 ± 12 versus 68 ± 8, $P < 0.0001$) and peritoneal macrophages (498 ± 59 versus 32 ± 13, $P < 0.0001$) than that from the macrophages isolated from WT mice (*SI Appendix*, Fig. S2 *E* and *F*), supporting the crucial role of Irp2 in the immune function of macrophages for pathogen clearance.

Macrophages and neutrophils are both critical phagocytes in the innate immune response to bacterial pathogens (24). Neutrophils, also expressing LysM and are myeloid derived, make up approximately 40 to 60% of white blood cells. Similarly, we explored the phagocytosis and bacteria-killing function of neutrophils. The results indicated no significant difference between WT and *Irp2*-deficient neutrophils after bacterial infection for 1 h and 4 h (*SI Appendix*, Fig. S2 *G* and *H*), suggesting that the bacterial-killing function of neutrophils was independent of *Irp2*. We therefore focused on Irp2 function in macrophages for the subsequent experiments.

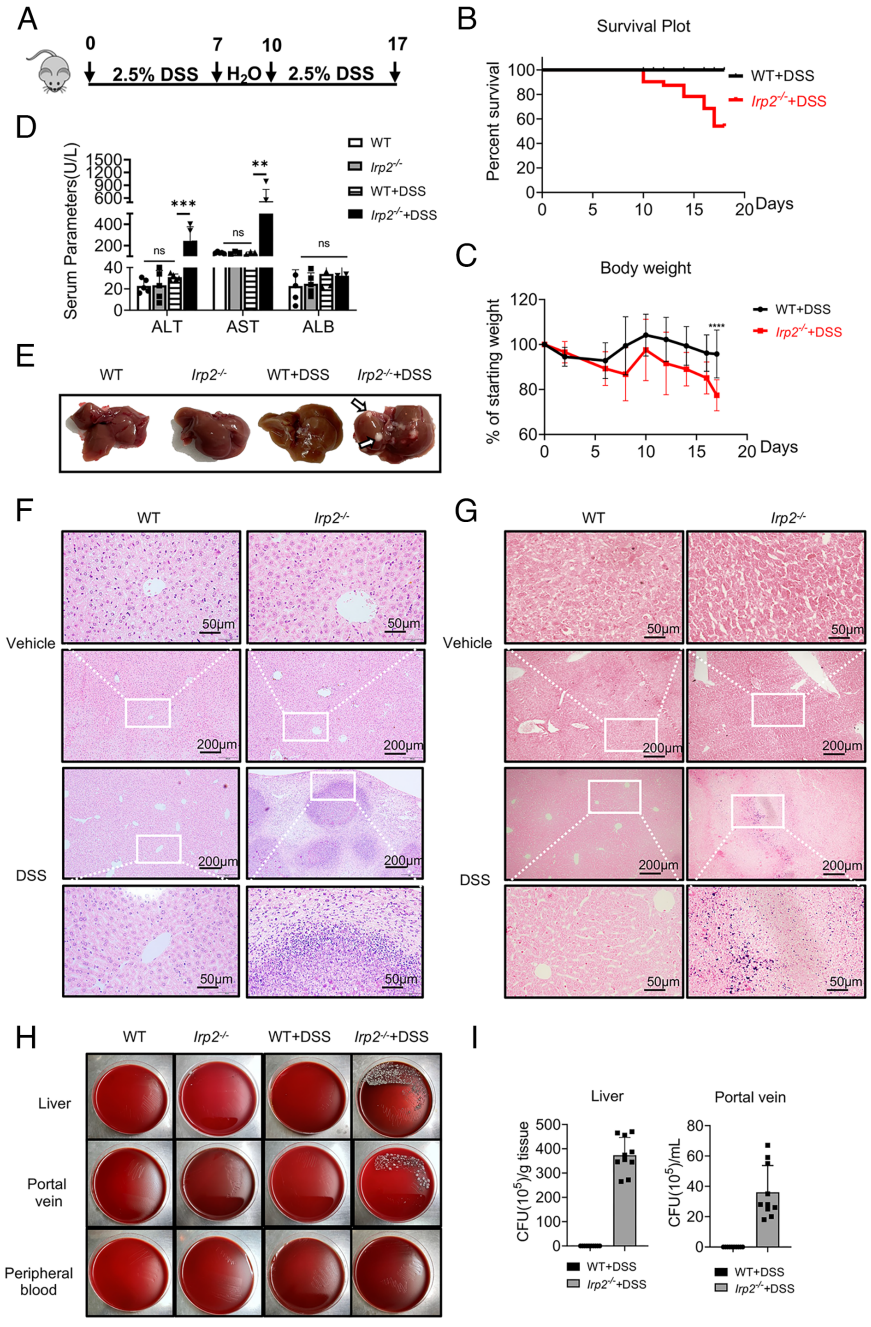

Fig. 1. Liver abscesses are induced by DSS treatment in *Irp2* KO mice. (*A*) Diagram showing the timing (in days) of treatment applications in the mouse model. (*B*) Survival plot of the animals during the treatment period (n = 30). (*C*) Body weight changes during the treatment period (initially n = 30, but some animals deceased). (*D*) Serum parameters for liver function. (*E*) The appearance of the liver of WT and *Irp2*$^{-/-}$ mice 17 d after initiation of DSS exposure. The white arrows indicated the sites of pus-filled lesions. (*F*) H&E staining of liver tissue. (*G*) Gram-staining of the liver. (*H*) Bacterial growth on blood agar plates from the liver, portal vein, and peripheral blood. (*I*) Quantification of the numbers of bacterial colonies in liver and portal vein blood after DSS exposure. n = 5/group if not specified. Data are presented as means ± SD. $^{**}P < 0.01$, $^{***}P < 0.001$, $^{****}P < 0.0001$. ns: no significance. ALT, Alanine aminotransferase; AST, Aspartate aminotransferase; ALB, Albumin. White boxes indicate the enlarged regions.

Lysosomal Biogenesis and Acidification Are Defective in *Irp2*$^{-/-}$ Macrophages. Phagolysosome trafficking is an important innate defense mechanism that removes microbes by delivering them to lysosomes. Acidic lysosomes must fuse to the pathogen-entrapped phagosomes in macrophages, a crucial step for pathogen clearance. To detect whether *Irp2* deficiency affects the fusion of lysosomes with phagosomes, we examined the colocalization of eGFP-*E. coli* with lysosome-associated membrane protein 1 (Lamp1), a typical lysosomal marker. As expected, bacteria were found to be associated with Lamp1-positive staining. However, no alteration of this association was observed in the absence or presence of *Irp2* in both BMDM and peritoneal macrophages (*SI Appendix*, Fig. S3 *A* and *B*). Since more bacteria survived in *Irp2*$^{-/-}$ BMDM and peritoneal macrophages (Fig. 3*A*), another explanation should exist of why Irp2 is required for the lysosomal function for bacteria clearance.

Lysosomal function relies on prior organelle biogenesis and maturation/acidification (25, 26). We thus wondered whether lysosomal biogenesis and maturation were affected by *Irp2* deficiency. Lamp1 and a lysosomal cysteine protease cathepsin B (Ctsb), two lysosomal constitutive components, were determined prior to and post *E. coli* infection. Immunoblot results showed that Lamp1 and Ctsb protein levels decreased in *Irp2*$^{-/-}$ macrophages compared to their WT counterparts, regardless of the bacterial infection (Fig. 3 *C* and *D*, quantified in *SI Appendix*, Fig. S3 *C* and *D*). Lamp1 immunofluorescence data also corroborated this lysosomal marker's diminished presence in *Irp2*$^{-/-}$ BMDM and peritoneal macrophages prior to infection (Fig. 3 *E* and *F*) and postinfection with *E. coli* (Fig. 3 *G* and *H*). The maturation of Ctsb into an active form requires lysosomal acidification. We measured the extent of lysosomal acidification using pHrodo and lysotracker, two reagents that accumulate in

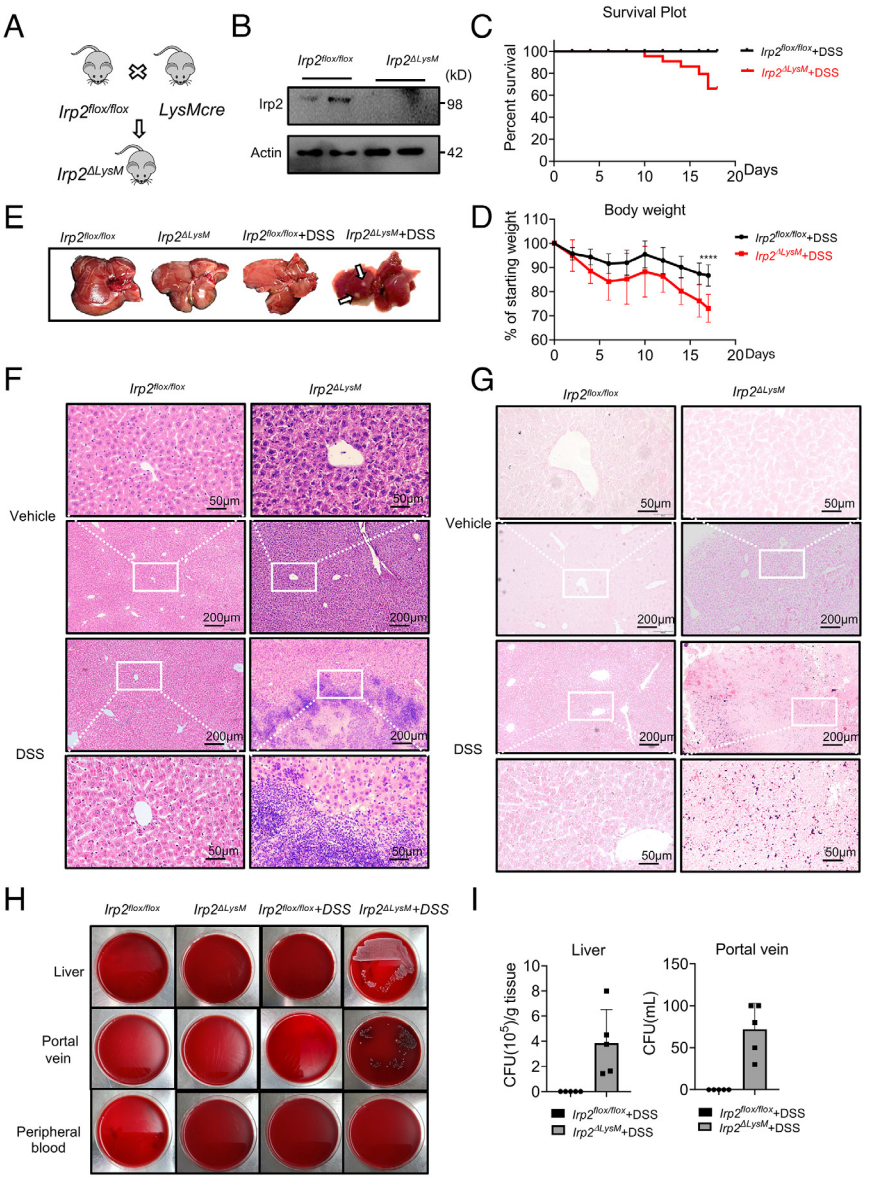

Fig. 2. *Irp2* deficiency in macrophages promotes DSS-induced liver abscesses. (*A*) Diagram showing the strategy to generate $Irp2^{\Delta LysM}$ mice. (*B*) Representative Western blotting demonstrating the *Irp2* KO in BMDM isolated from $Irp2^{\Delta LysM}$ and $Irp2^{flox/flox}$ mice. (*C*) Survival plot (n = 30). The experimental procedure was the same as in Fig. 1*A*. (*D*) Body weight changes post-DSS drinking (initially n = 30). (*E*) The appearance of the representative livers from WT and $Irp2^{\Delta LysM}$ mice with or without DSS treatment. White arrows indicated the sites of liver abscesses. (*F*) H&E staining of the liver sections. (*G*) Gram-positive staining with the liver sections. (*H*) Bacterial growth on blood agar plates from the liver, portal vein, and peripheral blood. (*I*) Quantification of the number of bacteria in liver tissue and portal vein blood after DSS treatment. n = 5/group if not specified. Data are means ± SD. ****P < 0.0001. White boxes indicate the enlarged regions.

lysosomes through a pH-dependent mechanism. The fluorescence intensity of pHrodo was attenuated in $Irp2^{-/-}$ BMDM and peritoneal macrophages (Fig. 3 *I* and *J*), and lysotracker's fluorescence intensity also decreased in $Irp2^{-/-}$ macrophages prior to and post bacterial infection (*SI Appendix*, Fig. S3 *D*–*G*). The results indicate that lysosomal biogenesis and acidification competence were attenuated in $Irp2^{-/-}$ macrophages.

***Irp2* Deletion Down-Regulates Transcript Levels and Nuclear Translocation of Transcription Factor EB (Tfeb) in Macrophages.** Since transcription factors of the MiTF/TFE family play a pivotal role in the regulation of lysosomal function and biogenesis (27), we examined the expression of the three family members, *Tfeb* (the basic helix–loop–helix leucine zipper transcription factor EB), *Tfe3* (transcription factor binding to Immunoglobulin Heavy Constant Mu enhancer 3), *Mitf* (melanocyte inducing transcription factor) and a subunit of H(+)-ATPases, *Atp6v0e2* (ATPase H+ transporting V0 subunit e2), an essential proton pump component. We found diminished mRNA levels in the liver of $Irp2^{-/-}$ mice of *Tfeb* and *Mitf* to approximately 50% of their WT levels, not so for *Tfe3* and *Atp6v0e2* (Fig. 4*A*). All four genes expressed significantly less in the $Irp2^{-/-}$ mutant than in WT following DSS treatment (Fig. 4*A*). Notably, the DSS treatment caused a rough 15-fold and 27-fold induction of *Tfe3* and *Atp6v0e2* in WT livers, whereas this response was entirely blunted in livers of $Irp2^{-/-}$ mice. To examine whether a similar response was expected in macrophages, as observed in the liver, we constructed *Irp2* KO RAW264.7 cells (RAW^{Irp2KO}, *SI Appendix*, Fig. S4*A*). In agreement with previous studies (28), *Irp2*-KO up-regulated FtH and hypoxia-inducible factor 2α (Hif2α) protein levels (*SI Appendix*, Fig. S4*B*). Consistent with the results in $Irp2^{-/-}$liver, *Tfeb* mRNA expression was also reduced in RAW^{Irp2KO} cells prior to and postinfection with *E. coli*, whereas the blunted response of *Tfe3* and *Atp6v0e2* postinfection was also observed (Fig. 4*B*), although these genes were not dramatically induced in cell culture. We then detected the protein levels of Tfeb and its downstream proteins, Lamp1 and Ctsb. Surprisingly, Tfeb protein levels were mildly higher in $Irp2^{-/-}$ liver and RAW^{Irp2KO} cells before DSS treatment or prior to *E. coli* infection (Fig. 4 *C* and *D*). However, protein levels of Lamp1 and Ctsb were both diminished in mutants compared to WT prior to DSS treatment or *E. coli* infection

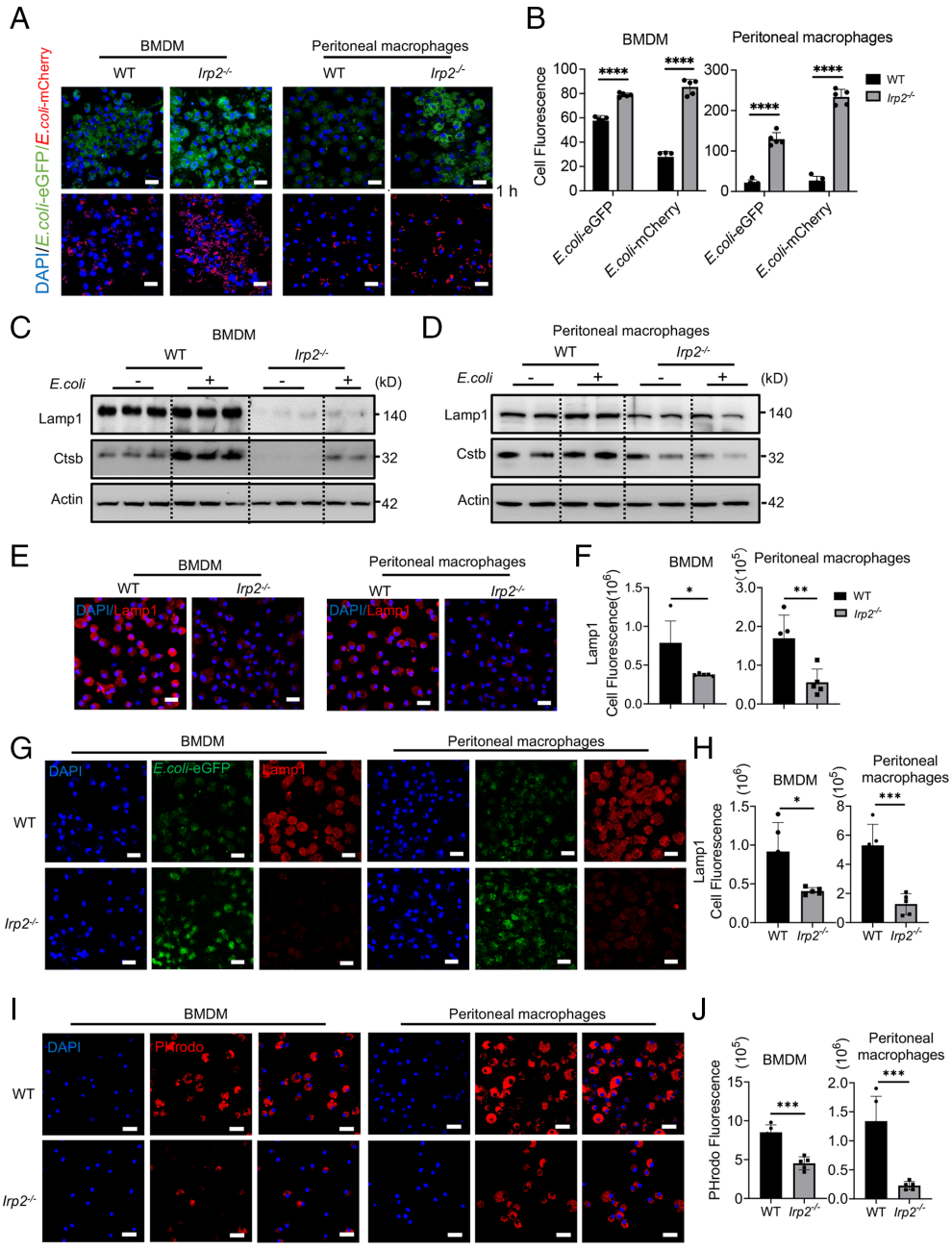

Fig. 3. The increased bacterial load and decreased bacterial clearance of *Irp2*$^{-/-}$ macrophages were associated with macrophage defective lysosomal biogenesis and acidification when infection by *E. coli*. (*A*) Confocal images of BMDM and peritoneal macrophages that were infected with eGFP-expressing (*E. coli*-eGFP) or mCherry-expressing *E. coli* (*E. coli*-mCherry) with MOI = 50 for 1 h. *E. coli* that were not phagocytosed were removed by gentamicin (200 μg/mL for 30 min). (*B*) Quantification of fluorescence, representing *E. coli*-eGFP and *E. coli*-mCherry in BMDM and peritoneal macrophages. (*C* and *D*) Protein levels of lysosomal markers Lamp1 and Ctsb in BMDM (*C*) and peritoneal macrophages (*D*) after incubation with *E. coli* with MOI = 10 for 90 min. (*E*) Lamp1 expression levels in BMDM and peritoneal macrophages of WT and *Irp2*$^{-/-}$ mutant as revealed by immunofluorescence assays. (*F*) Quantification for *E*. (*G*) Lamp1 expression levels in BMDM and peritoneal macrophages of WT and *Irp2*$^{-/-}$ mice post–*E. coli* infection, revealed by immunofluorescence assays. MOI = 50 for 1 h. (*H*) Quantification for *G*. (*I*) Lysosomal acidification in BMDM and peritoneal macrophages as indicated by pH-dependent pHrodo fluorescence. (*J*) The quantification of the fluorescence intensity of pHrodo for *I*. **P* < 0.05, ***P* < 0.01, ****P* < 0.001, *****P* < 0.0001. Scale bar, 20 μm.

(Fig. 4 *C* and *D*). Tfeb exerts its function via translocating into the nucleus, so we wondered whether the nuclear translocation was inhibited in *Irp2* mutants. Indeed, the nuclear fraction of Tfeb was significantly reduced, and cytosolic Tfeb was increased considerably in RAW^{Irp2KO} cells (Fig. 4*E*). As expected, Tfeb expression increased in the liver following DSS treatment and in RAW264.7 cells after *E. coli* infection, whereas the changes in Lamp1 and Ctsb were found only in WT, not in the *Irp2* mutants (Fig. 4 *C* and *D*, quantified in *SI Appendix*, Fig. S4 *C* and *D*). Consistently, the nuclear fraction of Tfeb was less in *Irp2* mutant than in WT (Fig. 4 *E* and *F*). To verify the conclusion further, we observed the localization of Tfeb in RAW^{Irp2KO} cells by confocal microscopy. Similarly, Tfeb was more localized in the nucleus in WT than in *Irp2* mutants, regardless of the infectious state (*SI Appendix*, Fig. S4 *E* and *F*). These results indicated that *Irp2* ablation impairs nuclear localization of transcription factor Tfeb and the expression of its target genes related to lysosomal biogenesis and function.

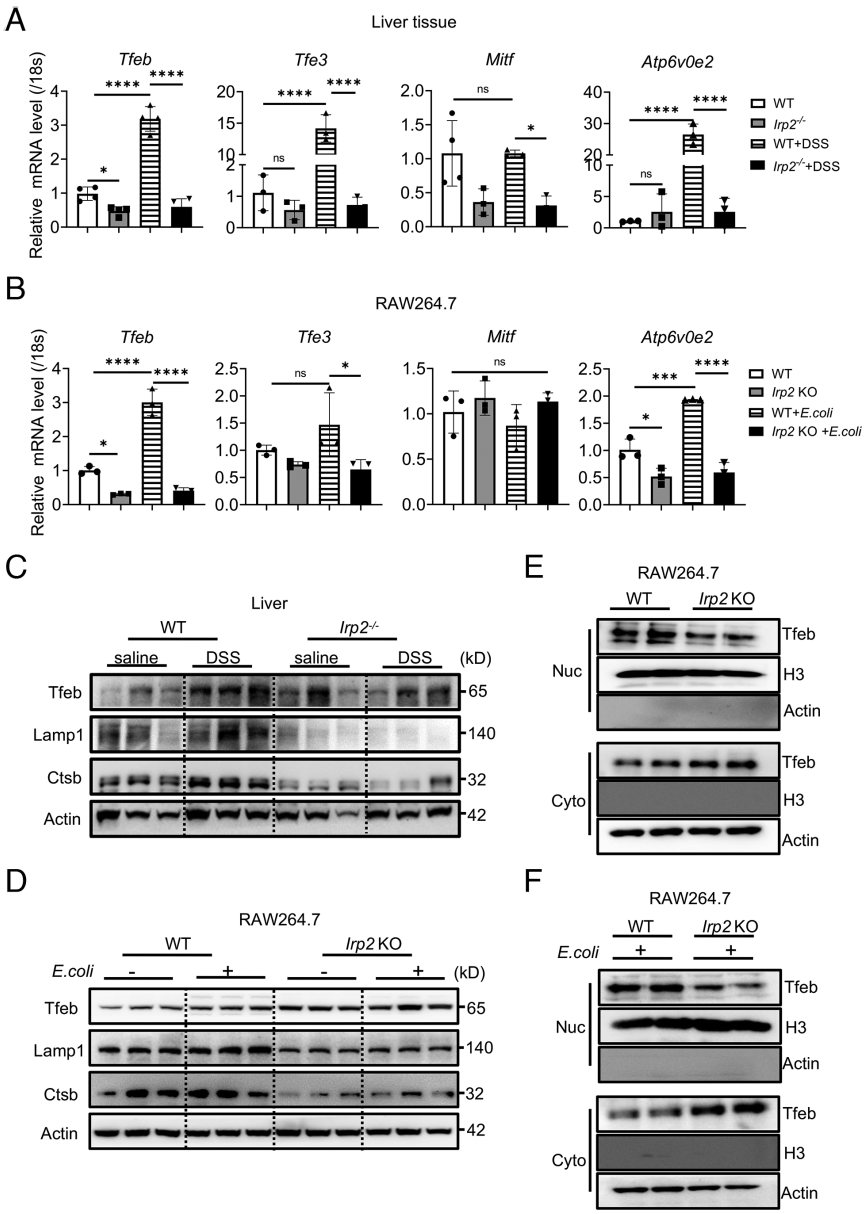

Fig. 4. Expression and nuclear localization of Tfeb decreases in *Irp2*$^{-/-}$ liver tissue and macrophages. (*A* and *B*) mRNA levels of the Mitf family members, *Tfeb, Tfe3,* and *Mitf,* and their target gene *Atp6v0e2* in the liver of mice treated with DSS water (*A*) and in macrophage-like RAW264.7 cells postinfection by *E. coli* (*B*). (*C* and *D*) Protein levels of Tfeb and its target protein Lamp1 and Ctsb in the liver of DSS-treated mice (*C*) and in RAW264.7 cells postinfection by *E. coli* (*D*). (*E* and *F*) Nuclear and cytosolic Tfeb in WT and RAW^{Irp2KO} cells before infection (*E*) and postinfection (*F*) with *E. coli*. MOI = 25 for 90 min. Results are expressed as means ± SD from three independent experiments. *P < 0.05, ***P < 0.001, ****P < 0.0001; ns: no significance.

***Irp2*-Deficiency Product Lactate Inhibits Tfeb Nuclear Localization Thereby Suppressing Lysosomal Biogenesis and Function in RAW264.7 Cells.** Our previous study demonstrated increased lactate production in *Irp2*$^{-/-}$murine embryonic fibroblasts (MEFs) (20) and *Irp2*$^{-/-}$tissues (29). Recently, it has been suggested that lactate production is coupled with the decrease in nuclear localization of Tfeb (30). We studied whether a similar phenomenon occurred in macrophages. First, we showed that lactic acid content in the medium increased in RAW^{Irp2KO} cells compared to WT cells and increased further after *E. coli* infection. In contrast, lactic acid remained constant in WT cells post *E. coli* infection (Fig. 5*A*). The increase in extracellular lactic acid could be reversed by treatment with 20 mM sodium oxamate (OXA), an inhibitor of lactic dehydrogenase A (LdhA), regardless of *E. coli* infection (*SI Appendix*, Fig. S5*A*).

We then tested the effects of OXA treatment on the immune function of macrophages against *E. coli* infection. The bacterial load was reduced in RAW^{Irp2KO} after OXA treatment (Fig. 5*B*). Then, we measured the effects of lactic acid on the protein levels of Tfeb, Lamp1, and Ctsb. We observed an increase in Tfeb after lactic acid treatment. On the contrary, its target protein levels of Lamp1 and Ctsb decreased no matter whether the cells were infected with *E. coli* or not (Fig. 5 *C* and *D*; for parallel measurements of lactic acid content see *SI Appendix*, Fig. 5*B*; protein levels quantified in *SI Appendix*, Fig. S5 *C* and *D*). To further demonstrate the regulatory role of lactic acid on Tfeb and its target genes, we treated WT and *Irp2* mutant cells with OXA to inhibit the production of lactic acid. After treatment, LdhA expression was reduced, and surprisingly, Tfeb expression decreased while Lamp1 and Ctsb were significantly increased, particularly in *Irp2* mutant cells (Fig. 5 *E* and *F*, quantified in *SI Appendix*, Fig. S5 *E* and *F*). Again, we prepared nuclear fractions and detected Tfeb nuclear localization after lactic acid or OXA treatment. Western blot results of cell fractions showed less nuclear and more cytosolic localization of Tfeb after lactic acid treatment in WT cells (Fig. 5*G*, quantified in *SI Appendix*, Fig. S5*G*). In contrast, OXA treatment reversed the Tfeb localization in the *Irp2* mutant (Fig. 5*H*, quantified in *SI Appendix*, Fig. S5*H*). The results indicated that the *Irp2* ablation-mediated induction of lactic acid play a crucial role in lysosomal biogenesis and function.

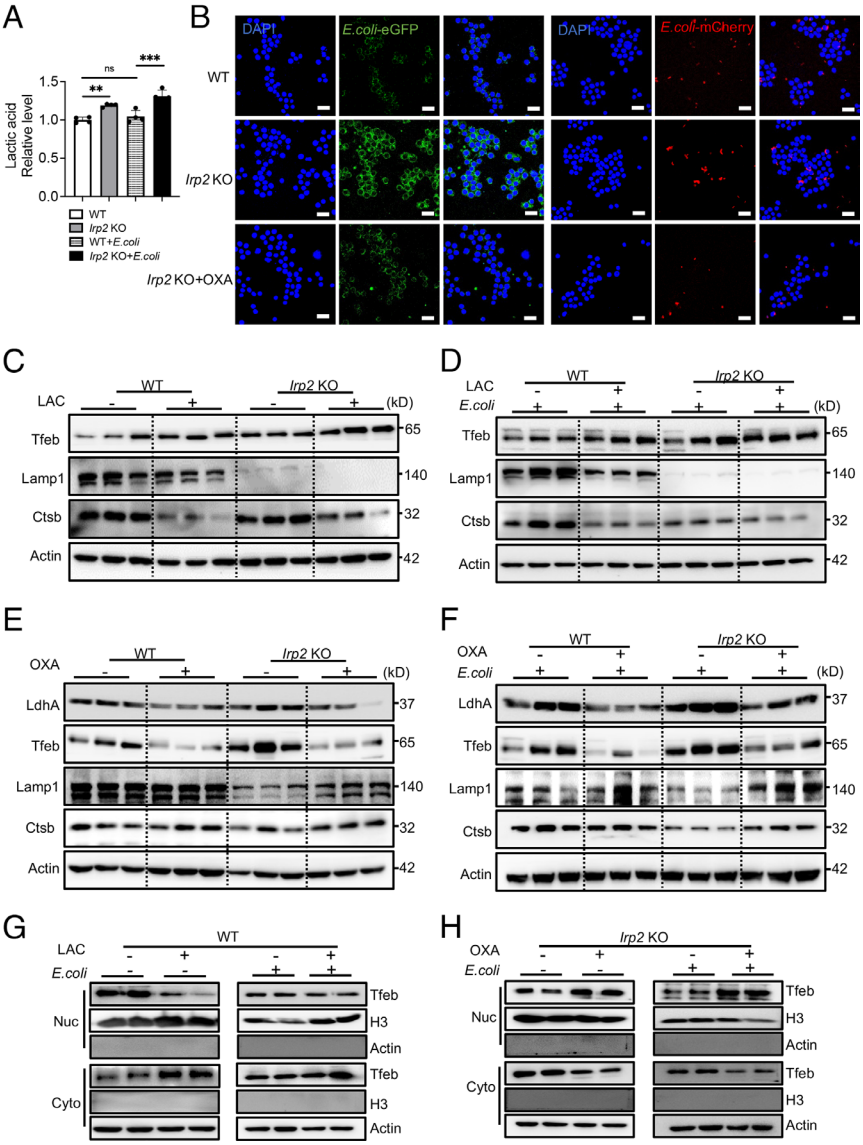

Fig. 5. *Irp2* deficiency-induced lactate suppresses lysosomal biogenesis and function in RAW264.7 cells by inhibiting Tfeb nuclear localization. (*A*) Lactate contents in WT and *Irp2*-deficient mutant culture medium prior to and post–*E. coli* infection. (*B*) Retained *E. coli*-eGFP and *E. coli*-mCherry in WT and RAW^{Irp2KO} cells pretreated with LdhA-specific inhibitor OXA (20 mM) for 30 min. (*C* and *D*) Western blots showing Tfeb and its target proteins following treatment with 5 mM lactic acid (LAC) prior to *C* and post–*E. coli* infection (*D*). (*E* and *F*) Protein levels of Tfeb and its target proteins posttreatment with 20 mM OXA prior to *E* and post–*E. coli* infection (*F*). (*G* and *H*) Nuclear and cytosolic Tfeb protein levels in WT treated with 5 mM lactic acid (*G*) or in *Irp2* KO treated with 20 mM OXA (*H*) followed by *E. coli* infection. Results are expressed as means ± SD from three independent experiments. $^{**}P < 0.01$, $^{***}P < 0.001$; ns: no significance.

Hif2α Inhibition Reverses the Bacterial Load in *Irp2* Deficient Cells and Mice by Reducing Lactic Acid Production. Our previous studies demonstrated that *Irp2* deficiency stabilizes Hif2α and increases lactic acid production in MEFs (20) and in the nervous system tissues of mice (29). Consistently, levels of Hif2α were elevated in the liver of *Irp2*$^{-/-}$ mice and further increased after DSS treatment (Fig. 6*A*, quantified in *SI Appendix*, Fig. S6*A*). We wondered whether the expression of Hif2α was stabilized and lactic acid production increased in RAW^{Irp2KO} cells and showed that this is also the case (Fig. 6*B*, quantified in *SI Appendix*, Fig. S6*B*), supporting the idea that high production of lactic acid is derived from increased LdhA through its upregulation of Hif2α in *Irp2*-depleted cells (29). Then, we treated RAW^{Irp2KO} cells with PT2385, a compound that selectively disrupts the heterodimerization of Hif2α with Hif1β. The bacterial load was significantly lessened in *Irp2*-depletion macrophages after 1 h infection by *E. coli* with PT2385 treatment (Fig. 6*C*, quantified in *SI Appendix*, Fig. S6*C*). Accordingly, the lactic acid content was reversed significantly in the *Irp2* mutant after PT2385 treatment regardless of infection (*SI Appendix*, Fig. S6*D*). PT2385 treatment increased the protein levels of Lamp1 and Ctsb under both infection and noninfection conditions (*SI Appendix*, Fig. S6 *E*–*G*). Accordingly, Tfeb nuclear localization increased significantly at the expense of Tfeb cytoplasmic localization following PT2385 treatment (*SI Appendix*, Fig. S6 *H*–*J*). Similarly, we isolated the BMDM and peritoneal macrophages from *Irp2*$^{flox/flox}$ and *Irp2*$^{\Delta LysM}$ mice to measure the mRNA expression of *Tfeb, Tfe3, and Atp6v0e2*, the lactic content, and levels of Hif2α and lysosome-related proteins before and after bacterial infection (*SI Appendix*, Fig. S7 *A*–*D*). All the results were consistent with those already described from RAW^{Irp2KO} cells, adding evidence for the crucial role of Irp2 in the lysosomal function of macrophages through Hif2α and LdhA expression to control lactic acid production.

To further test these conclusions in vivo, we treated *Irp2*$^{\Delta LysM}$ mice with PT2385 every other day for 2 wk and then exposed the animals to 2.5% DSS treatment (Fig. 6*D*). Body weight loss was significantly reversed after PT2385 treatment in *Irp2*$^{\Delta LysM}$(Fig. 6*E*), and survival rate improved considerably (Fig. 6*F*). Importantly, the gross pus-filled appearance of liver abscesses disappeared after PT2385 treatment in *Irp2*$^{\Delta LysM}$mice (Fig. 6*G*); H&E and gram-positive staining indicated the liver abscesses were attenuated after treatment (Fig. 6 *H* and *I*). The blood agar cultures further verified the protective effects of PT2385 from pathogen infection in *Irp2*$^{\Delta LysM}$mice (Fig. 6*J*, quantified in *SI Appendix*, Fig. S7*E*). Thus, the in vivo evidence also supports our conclusion that Irp2 functions in macrophage immunity as a

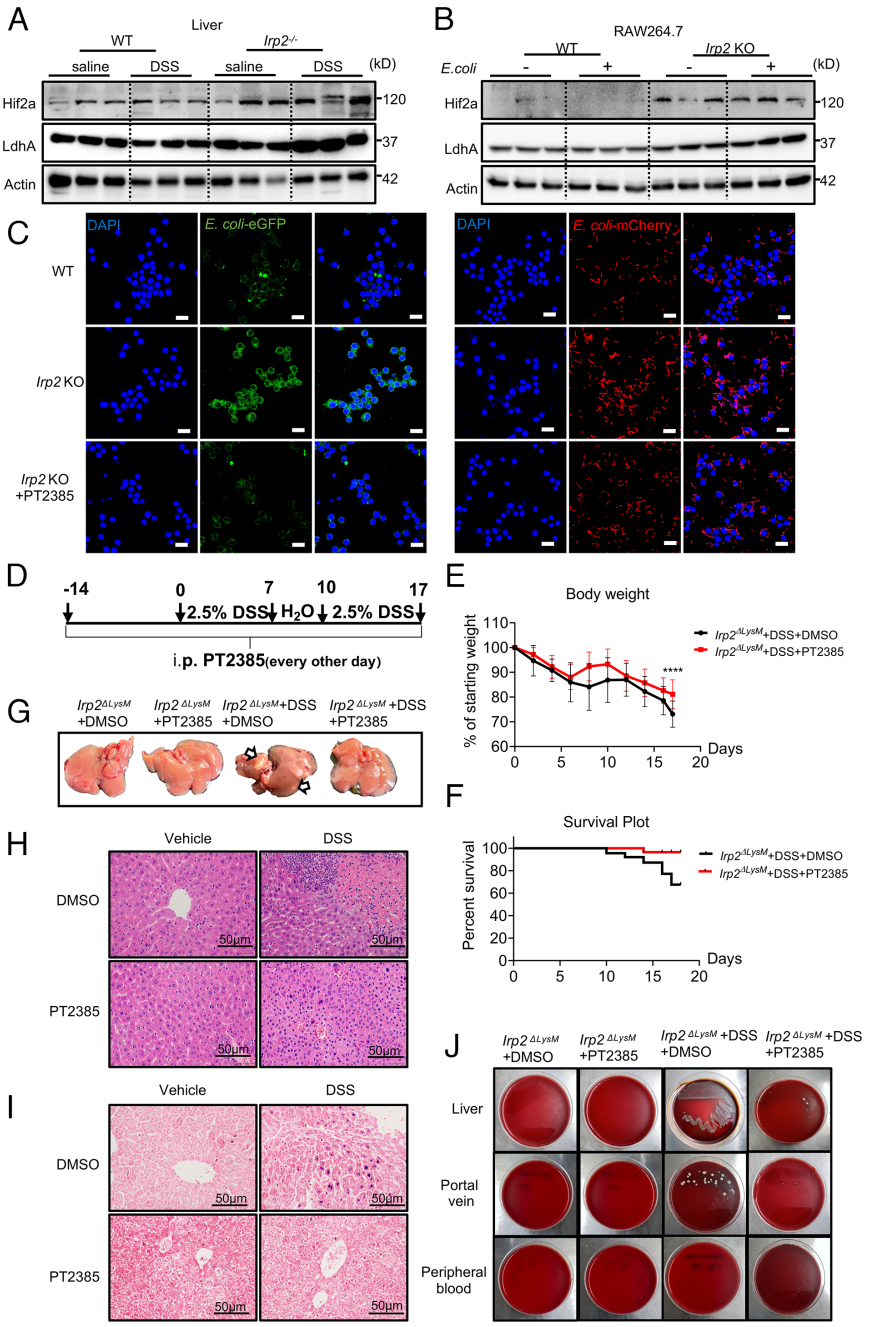

Fig. 6. Irp2 restrains Hif2α expression, promoting lysosomal biogenesis and function in the macrophage's immune responses against bacterial infection. (*A* and *B*) Hif2α and LdhA protein levels in WT and $Irp2^{-/-}$ liver after DSS modeling (*A*) and in WT and RAW^{Irp2KO} cells after *E. coli* infection (*B*), revealed by immunoblotting assays. (*C*) Retained *E. coli*-eGFP and *E. coli*-mCherry in WT and RAW^{Irp2KO} cells, pretreated with Hif2 specific inhibitor PT2385. (*D*) Diagram of PT2385 administration during the treatment protocol. (*E*) Body weight changes following administration of PT2385 (initially n = 30). (*F*) Survival plot of the animals during the protocol's duration (n = 30). (*G*) Gross appearance of representative livers from $Irp2^{\Delta LysM}$ mice after treatment with PT2385 in the DSS-induced IBD model. White arrows indicate the sites of abscesses. (*H*) H&E staining of the liver. (*I*) Gram-positive staining of the liver. (*J*) Bacterial growth from the liver, portal vein blood, and peripheral blood on blood agar plates. n = 5/group if not specified. Data are presented as means ± SD. ****$P < 0.0001$.

negative regulator of Hif2α. Furthermore, pharmacologic prevention of Hif2 activation is protective against the formation of liver abscesses, and this is because lactic acid production is inhibited and Tfeb nuclear translocation permits normal lysosomal biogenesis and function.

IRP2 Expression Is Down-Regulated in the Intestine of Crohn's Disease Patients. We have demonstrated that the liver abscesses result from intestinal injury in *Irp2*-ablated mice and is accompanied by Tfeb subcellular mislocalization in macrophages. To examine the expression of IRP2 and TFEB in patients with Crohn's disease, we collected resected tissue samples. The mRNA levels of *IRP2* and *TFEB* were significantly reduced in lesion regions compared with nonlesion parts of the intestine from the same patients (Fig. 7*A*). IRP2 protein levels were reduced, while TFEB increased in lesion regions despite the loss of encoding mRNA (Fig. 7 *B* and *C*), matching well with the observations in mice and cell culture. Immunoblotting assays consistently confirmed the decrease in IRP2 and increase in TFEB protein levels, and Hif2α and LdhA were increasingly accumulating in lesion regions (Fig. 7*D*, quantified on the *Right*). To expand the relevance of these observations to a larger set of clinical samples, we searched the GEO database of ulcerative colitis and Crohn's disease. The extracted data revealed a significant reduction of *IRP2* and *TFEB* mRNA expression in Crohn's disease and ulcerative colitis, compared with the normal tissues (*SI Appendix*, Fig. S7*F*). Thus, the clinical data from our collection and data from clinical databases agree with that IRP2 insufficiency might be a high-risk clinical factor in developing ulcerative colitis and Crohn's disease, potentially also in developing PLAs in the absence of protective interventions.

Discussion

In this study, we demonstrated that Irp2 is required in macrophages to support a functional immune response (Fig. 8). Deletion of *Irp2* globally or *LysM*-specifically caused the appearance of liver abscesses

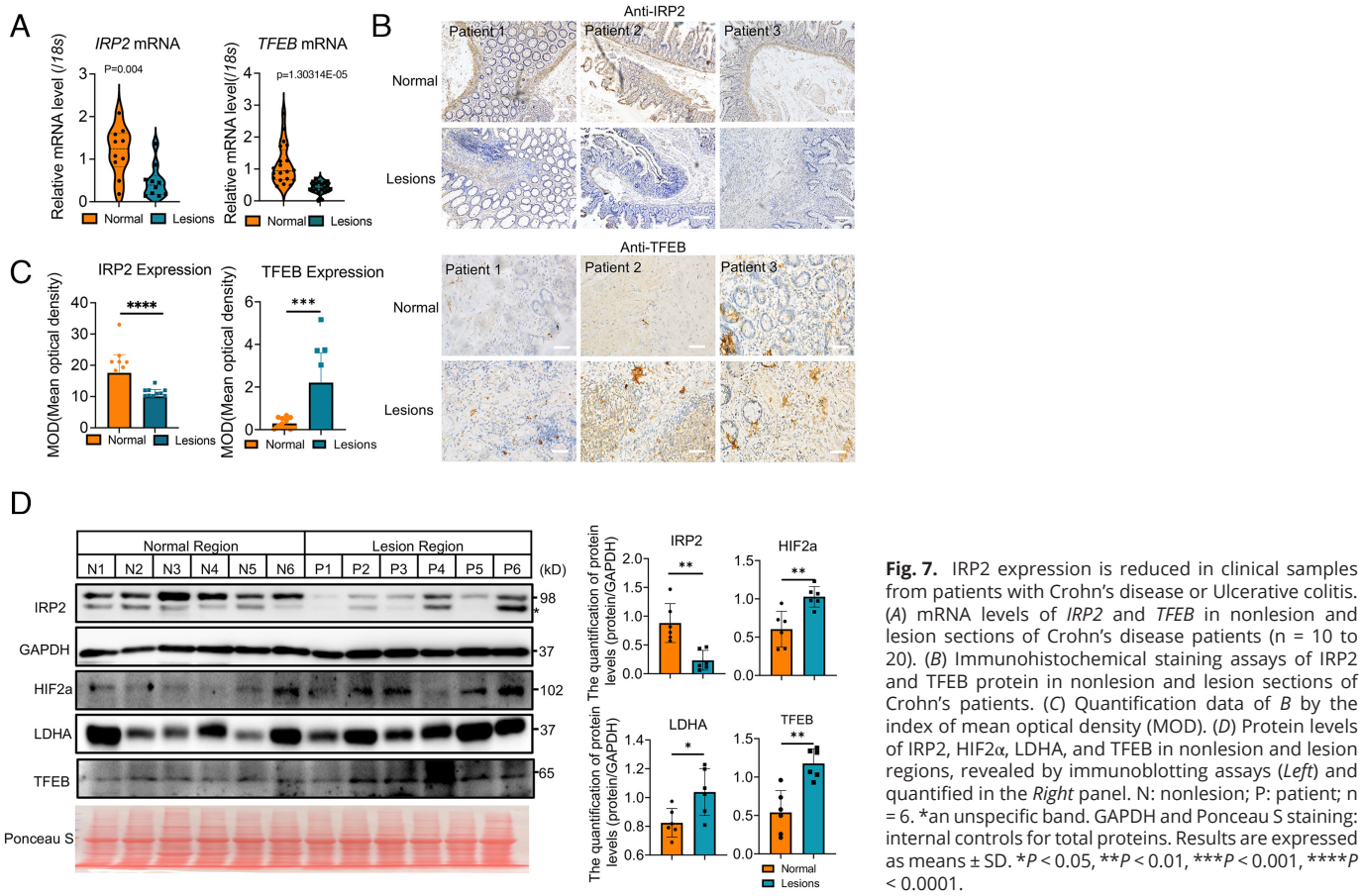

Fig. 7. IRP2 expression is reduced in clinical samples from patients with Crohn's disease or Ulcerative colitis. (*A*) mRNA levels of *IRP2* and *TFEB* in nonlesion and lesion sections of Crohn's disease patients (n = 10 to 20). (*B*) Immunohistochemical staining assays of IRP2 and TFEB protein in nonlesion and lesion sections of Crohn's patients. (*C*) Quantification data of *B* by the index of mean optical density (MOD). (*D*) Protein levels of IRP2, HIF2α, LDHA, and TFEB in nonlesion and lesion regions, revealed by immunoblotting assays (*Left*) and quantified in the *Right* panel. N: nonlesion; P: patient; n = 6. *an unspecific band. GAPDH and Ponceau S staining: internal controls for total proteins. Results are expressed as means ± SD. $*P < 0.05$, $**P < 0.01$, $***P < 0.001$, $****P < 0.0001$.

in the DSS-induced IBD model. Following our previous study, where we showed that *Irp2* deficiency induces Hif2α, which turns on LdhA expression, resulting in more lactic acid production (20), we found here that the increase in lactic acid retains Tfeb in the cytosol, rather than its functional presence in the nucleus. Consequently, macrophage function is compromised, resulting in pathogen infection and liver abscesses, a lethal condition both in mice and in human patients.

Decades ago, a few case reports revealed that PLAs are connected to various colonic diseases, such as IBDs (31–33), and more recently, additional cases have been reported (6, 10). It is believed that the mucosal barrier separating enteric bacteria from the circulation allows a route for bacteria invasion into the portal system, with subsequent hematogenous spread to the liver (11). Located in the subepithelial lamina propria close to vast numbers of luminal bacteria and antigenic stimuli, gut macrophages are part of the first-line defense mechanisms in protecting the mucosa against harmful pathogens (34). The liver functions as a second firewall through a slow-flowing vascular system that could harbor antigens without translocation toward lymph nodes (35). The Kupffer cells in the liver sinusoids are located in an optimal position to clear bacteria, while increased gut leakage exhausts the scavenging capacity of Kupffer cells (36). In this case, the number of Kupffer cells decreases, and the recruitment and infiltration of monocytes to the liver increase, suggesting the vital role of monocyte-derived macrophages in the gut–liver axis (37, 38). In our study, the DSS-induced liver abscess in both $Irp2^{-/-}$ and $Irp2^{\Delta LysM}$ indicates the crucial role of Irp2 in monocyte-derived macrophages. We have not excluded the role of Irp2 in other cell types (including hepatocytes, Kupffer cells, or intestinal epithelial cells). Although mice with hepatocyte-specific *Irp2* deficiency display normal red blood cell and plasma iron parameters (39), the responses of the hepatocytes to inflammation or pathogen infection are still unknown. In the scenario of this study, mice with DSS treatment or patients with IBD bear intestinal epithelial injury, and the intestinal barrier integrity is compromised, which is considered to contribute to IBD (40).

Lysosome-mediated clearance of pathogens by macrophages is critically defective in IBD (reviewed in refs. 12 and 41). TFEB, one of the MiT/TFE family members harboring the coordinated lysosomal expression and regulation network motif, regulates lysosomal biogenesis and function (42–44). It has been demonstrated that TFEB is linked to an increased risk of developing colitis (reviewed in ref. 45). In this study, we showed that the lysosomal function and competence of bacterial killing were compromised mainly due to the defective translocation of Tfeb and associated impaired lysosomal acidification in *Irp2*-deficient macrophages. Disruption of lysosomal acidity has been previously shown to trigger functional iron deficiency, resulting in Hif1/2 upregulation and mitochondrial dysfunction (46, 47). This mutual interaction suggests the strong physiologic coupling between lysosomal acidity and iron homeostasis, while Irp2 function reestablishes iron homeostasis ensuring lysosomal biogenesis through Tfeb activation (nuclear translocation). Although *Irp2* deficiency causes liver iron accumulation (19, 20, 28, 39) (*SI Appendix*, Fig. S8 *A* and *B*), ferric iron is found in ferritin causing a functional iron deficiency, as demonstrated in fibroblast/macrophages (19, 20, 28, 39) (*SI Appendix*, Fig. S8 *C* and *D*). Thus, Hif2a is up-regulated and induces LdhA causing the production of lactic acid. Inhibition of Hif2 reverses all phenotypes. Additionally, to see whether iron addition on its own would reverse macrophage lysosomal biogenesis and function, we measured the related proteins, Lamp1 and Ctsb, and showed no improvement (*SI Appendix*, Fig. S8 *E* and *F*).

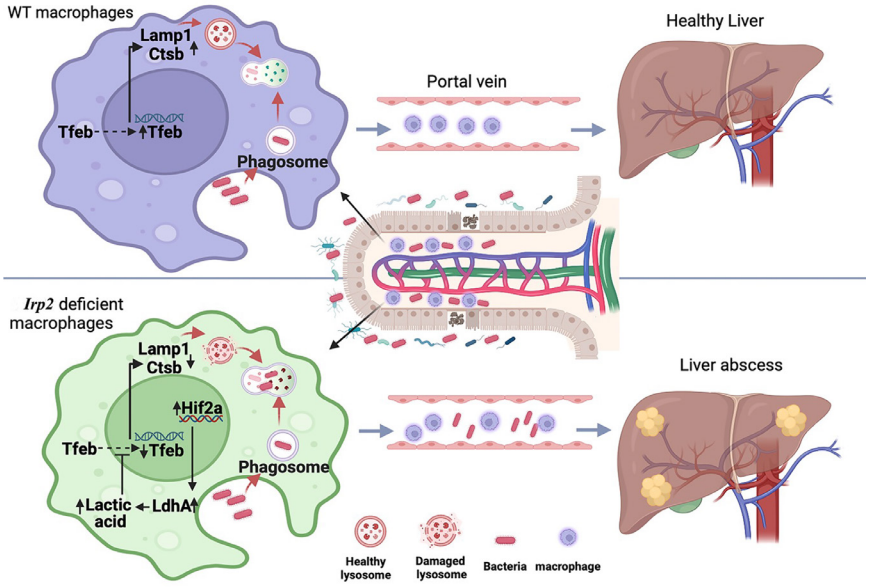

Fig. 8. A schematic model presenting IRP2 functions in macrophages leading to prevention from developing liver abscesses in the context of intestinal barrier injury. Irp2 preserves lysosomal biogenesis and function by regulating Tfeb nuclear localization in macrophages. *Irp2* deficiency up-regulates Hif2a expression, which induces lactic acid production by targeting LdhA genes. The increased lactic acid mislocalizes Tfeb, a key transcription factor to regulate a series of lysosome genes. Thus, macrophage lysosomal function is compromised, giving the pathogens a chance to route into the portal vein from the injured intestinal barrier. The constant pathogen invasion and translocation into the liver will promote the development of liver abscesses. (The scheme is created in BioRender.com).

This result also makes sense as Hif2a responds to both iron and oxygen. Irp2 is required for this dual response and regulates iron homeostasis and lysosome function in parallel.

As expected from prior work on *Irp2* deficient mice (20, 29), lactic acid accumulated in *Irp2*-ablated macrophages, resulting from Hif2α (not Hif1α) mediated LdhA upregulation (Fig. 6 and *SI Appendix*, Fig. S9 *A* and *B*). Lactic acid has been found to block the interaction between Rheb-Guanosine triphosphate (GTP) and GTPase activating Tuberous sclerosis complex 1 and 2 (TSC1 and TSC2) to preserve the Rheb-GTP levels and activate mTORC1 signaling (48). mTORC1 directly phosphorylates TFEB to keep TFEB cytosolic localization (49) by physical interaction (50). Inactivation of mTORC1 makes TFEB unphosphorylated and lets TFEB enter the nucleus for lysosomal gene expression (49). In agreement with these findings, we propose that the observed loss of nuclear Tfeb localization results from *Irp2* deficiency–induced lactate production. Indeed, blockage of lactate production increased Tfeb nuclear localization in *Irp2*-ablated macrophages. Inhibition of LDHA in macrophages was also shown to down-regulate proinflammatory cytokines and, therefore, exert anti-inflammatory effects (51), consistent with our observations.

A few studies have demonstrated that IRP1 down-regulates Hif2α through IRP–IRE binding within the 5′-UTR of the Hif2α mRNA (52, 53). However, Irp1 expression is either mild or compensatory elevated in *Irp2* KO mice (29). Whether Irp1 or Irp2-dependent Hif2α regulation is cell-type specific is unknown. Due to the significant increase of Hif2α in *Irp2* deficient macrophages and livers, we treated $Irp2^{-/-}$ mice with PT2385 before IBD modeling. This treatment mitigated the weight loss and surprisingly rescued all the *Irp2* ablation mice from liver abscess, supporting that Irp2 deficient-induced Hif2α might also be through the IRP–IRE binding pathway (54). Clinically, the IBD patient's immunocompromised state likely contributes to the development of liver abscesses, and a gut–liver link was reported many times (6, 10, 32, 33). Infliximab, a chimeric anti-tumour-necrosis factor-α monoclonal antibody, is a commonly used drug for the treatment of IBD. However, infliximab may enhance liver damage that promotes bacterial growth, as it causes hepatotoxicity, autoimmune hepatocellular injury, and transaminitis in patients with ulcerative colitis (55). Hif2α inhibitors were reported beneficial for treating Crohn's disease (56), supporting our findings here and suggesting their pharmaceutical use in IBD.

Irp2 deficiency in mice causes microcytic anemia and neurodegeneration due to functional cellular iron depletion (57–59), and Hif2 inhibition alleviates both manifestations (28, 29). This study expands the role of Irp2-Hif2 into the innate immunity relevant to lysosomal function, showing that Irp2 affects lysosomal biosynthesis and acidification of macrophages in defense against pathogen infection. Thus, Hif2a inhibitors likely have therapeutic applications in the treatment of IBD and its complications.

Materials and Methods

Participants. This study included 20 patients with bowel resection for Crohn's disease, aged 16 to 65. Participants were recruited from the Department of General Surgery, Jinling Hospital, Affiliated Hospital of Nanjing University Medical School in 2023 (*SI Appendix*, Table S1). Intestinal samples containing the injured segments and the resection margin were collected and separated into two parts: one snap-frozen and stored at −80 °C for further use and another fixed in 4% phosphate-buffered formalin and embedded in paraffin for histological analysis. This study complies with the Declaration of Helsinki and was approved by the Institutional Review Board (IRB) of Nanjing University Medical School. The IRB ensures that informed consent was properly obtained and all patients provided written informed consent. The study is conducted in accordance with ethical guidelines and regulations.

Animals and Genotyping. All experiments with rodents were performed according to the NIH Guide for the Care and Use of Laboratory Animals and were approved by the Animal Experimentation Administration of Nanjing University. The mice were fed a standard rodent diet, maintained in a constant 12-h light/dark cycle, and had access to food and water ad libitum. C57BL/6 $Irp2^{+/-}$ mice were purchased from MMRRC at UC Davis, United States, Cat. No. 030490-MU, and $Irp2^{-/-}$ mice were acquired by breeding $Irp2^{+/-}$ heterozygous mice. To obtain $Irp2^{\Delta LysM}$ mice, mating between *LysM*-Cre mice and control $Irp2^{flox/flox}$ mice (Cyagen Biosciences, Suzhou, China) was carried out. Mouse DNA was extracted following instructions (Mouse Tissue Lysis Kit, APExBIO). The primers for PCR genotyping are as follows: forward 5′-TTTACCATTTGGCCCCTGACAAC-3′; reverse 5′-TACAGCCAAAACATAGTCTAGAGGT-3′.

Reagents and Antibodies. The information on the primary antibodies used in this work is as follows: We obtained anti-Cathepsin B (CTSB) (cat#31718) from Cell Signaling Technology Inc. (Shanghai, China). We obtained anti-CTSB (cat#31718), anti-LAMP1 (cat#67300-1-Ig), and anti-TFEB (cat#13372-1-AP) from Proteintech Group Inc. (Wuhan, China). We obtained anti-Actin Beta (cat#66009-1-Ig) and anti-hif2a (cat#ab109616) from Abcam. We obtained anti-ferritin and anti-IRP2, which were self-made and validated in previous studies (20, 60). Secondary antibodies purchased

from Life Technologies included anti-mouse or anti-rabbit conjugated to horseradish peroxidase for Western blots and anti-rabbit conjugated to Alexa Fluor™ 594 and anti-mouse conjugated to Alexa Fluor™ 488 for confocal microscopy.

Other reagents used in this work include lactic acid from Sinopharm (Shanghai, China), sodium oxamate from MACKLIN, HIF2 inhibitor PT2385 from MedChemExpress (Shanghai, China), Lysotracker from Beyotime, and pHrodo from Life Technology.

DSS-Induced Liver Abscess Modeling and Drug Administration. For the liver abscess model, 7- to 9-wk-old mice were treated with 2.5% DSS (Yeasen Biotech Co., Ltd., Shanghai, China) for a week, followed by a 3-d interval with water and an additional week with 2.5% DSS. After 17 d, mice were killed by avertin for about 5 min. Tissues and blood were collected immediately thereafter.

For drug intervention, mice were divided into four groups: $Irp2^{\Delta LysM}$ mice with or without DSS plus vehicle DMSO ($Irp2^{\Delta LysM}$ ±DSS+DMSO) and $Irp2^{\Delta LysM}$ mice with or without DSS plus PT2385 ($Irp2^{\Delta LysM}$±DSS+PT2385, 0.4 mg/kg). PT2385 was dissolved in DMSO, diluted with normal saline, and injected intraperitoneally into 7 to 9-wk-old male mice for 2 wk and then treated with DSS (2.5%), same as for the DSS-induced liver abscess model. The vehicle DMSO or PT2385 was given every other day.

Cell Lines and Cell Culture. The murine macrophage cell line RAW264.7 was obtained from the American Type Culture Collection and cultured in Dulbecco's modified Eagle's Medium (DMEM) (Biosharp) supplemented with 10% fetal bovine serum (FBS) and penicillin (100 U/mL), and streptomycin (100 mg/mL) at 37 °C in 5% CO_2 incubator.

Histological Assays and Gram-Staining. H&E staining was performed as previously described (61). Tissue sections were treated with dewaxing and hydrating steps, followed by staining with hematoxylin for 5 min, then Eosin Y for 5 min. Sections of human intestine tissue were used to assess the protein levels of IRP2 and TFEB by immunohistochemical assays. The tissues were probed with primary antibodies followed by horseradish peroxidase–labeled secondary antibodies and staining with 3,3′-diaminobenzidine enhancement. The Gram-positive staining was operated according to the Gram-staining kit (Servicebio Technology Co. Ltd.). Images were captured under a light microscope (Olympus, Tokyo, Japan). The positive signal intensity was analyzed using NIH Image J software.

Western Blots. Cells or tissues were harvested and washed with ice-cold phosphate-buffered saline (PBS) and lysed in lysis buffer as previously described (61). The protein concentrations of lysates were measured using a standard Branford assay. For Western blots, 15 to 60 μg of protein from the whole cell lysate was electrophoresed by sodium dodecyl sulfate polyacrylamide gel electrophoresis. The separated proteins were transferred from the acrylamide gel onto the nitrocellulose membrane probed with primary antibodies followed by horseradish peroxidase–labeled secondary antibodies according to the standard methodologies (61). The proteins were visualized using enhanced chemiluminescence and imaged by the digital Western blot imaging system (Tanon). Band intensity was quantified by NIH ImageJ software.

RT-qPCR. Total RNA was extracted by TRIzol (Vazyme Biotech Co. Ltd., Nanjing, China) and then reverse-transcribed into complementary DNA by HiScript III RT SuperMix for qPCR (Vazyme Biotech Co. Ltd.). mRNA expression of Mitf/Tfeb family genes and downstream genes were measured by quantitative PCR with ChamQ SYBR qPCR Master Mix (Vazyme Biotech Co. Ltd.) using the primers shown in *SI Appendix*, Table S2. 18S rRNA was used as an internal control. The relative mRNA expression levels were calculated by the delta–delta C_T method.

Isolation of Primary Macrophages and Neutrophils. BMDMs and peritoneal macrophages were isolated and cultured as described previously (62). Briefly, 7 to 9-wk-old mice were euthanized. Legs were dissected, and bone marrow was extracted from the tibia and femur bones after removing surrounding muscle under an aseptic condition. Bone marrow cells were collected and filtered using a 70 μM cell strainer. The cell suspension was centrifuged at 400× g for 5 min at room temperature, and the cell pellet was incubated in Ammonium-Chloride-Potassium lysing buffer (NH_4Cl 150 mM, $KHCO_3$ 10 mM, Ethylenediaminetetraacetic acid 0.1 mM pH7.4) for 5 min to remove red blood cells. To elicit the differentiation of bone marrow progenitor cells into BMDM, the cells were cultured in DMEM with colony-stimulating factor (Peprotech, Cranbury, NJ). Cells were cultured for 7 d for further experiments.

For peritoneal macrophage isolation, the mice were intraperitoneally injected with 4% starch broth (NaCl 0.5 g, beef extract 0.3 g, peptone 1.0 g, and starch 3.0 g in 100 mL of distilled H_2O) 3 d before the mice were killed. After anesthesia, the abdominal skin was carefully cut to 1 cm, and 5 to 8 mL PBS with 3% FBS was injected into the enterocele. After 10 min massage, the extract was centrifuged (400× g, 5 min). The sediment was then plated into plates for attachment or cryopreserved for further assays.

The mouse neutrophils from bone marrow were prepared by the methods described previously (63). Briefly, the mice were executed and bone marrow cells were collected. Cells suspension was centrifuged and then treated on a 78%, 69%, and 52% Percoll gradient. The neutrophils were obtained for further assays.

Gene KO by CRISPR/Cas9 in Cells. The *Irp2* targeting 20 bp guide RNA (gRNA) sequence were as follows: Forward: 5′-CACCGAGTTACTCTTACTTTACCAG-3′; Reverse: 5′-AAACCTGGTAAAGTAAGAGTAACTC-3′.

The gRNA sequences targeting the *Irp2* gene were cloned into the vector expressing Cas9 nuclease to construct the CRISPR/Cas9 KO plasmid and transfected into RAW264.7 cells using a liposome transfection kit (Yeasen Biotech Co., Ltd.). After transfection, single clones (RAW^{Irp2KO}) are selected with 0.4 mg/mL puromycin, and the genomic DNA is extracted for PCR and sequencing to confirm the KO. Total RNA and proteins were extracted to validate the KO by qPCR and Western blot. The impact of *Irp2* KO on the expression of iron metabolism-related genes was examined for functional validation.

Immunofluorescence Assays. Cells were seeded on coverslips until 70% confluence. Bacteria-treated cells were then fixed with 4% formaldehyde solution for 10 min at room temperature. After fixation, cells were washed twice with PBS and incubated with 0.2% Triton X-100 for 10 min to destroy the cell membrane. Cells were then incubated with blocking buffer (1% Bovine Serum Albumin in PBS) for 60 min and subsequently incubated with primary antibody overnight. Afterward, slips were incubated with a secondary antibody for 3 h at room temperature. Images were captured by a confocal laser microscope (Olympus FV3000, Tokyo, Japan) and analyzed using NIH ImageJ software.

Macrophage and Neutrophil Phagocytosis Assays. Macrophages were plated in 24-well plates. FITC-dextran (250 μg/mL) or *E. coli* expressing eGFP/mCherry were added to each well at a multiplicity of infection (MOI) of 10 to 50 and incubated at 37 °C for 15 min for phagocytosis assays and 60 min for clearance assays. Neutrophils were plated in 24-well plates and infected with *E. coli* expressing eGFP/mCherry at a MOI of 50 and incubated at 37 °C for 1 h for phagocytosis assays and 4 h for clearance assays. Subsequently, cells were washed 3 times with PBS and treated with gentamycin (100 to 200 μg/mL) at 37 °C for 30 min to remove extracellular bacteria if needed. The fluorescence intensity was measured by confocal laser microscopy. Bacterial colonies were counted after incubation at 37 °C for 24 h on LB plates.

For bacterial load assays, macrophages were lysed by adding 0.02% Triton X-100 for 10 min, and the lysate was smeared onto LB-agar. Bacterial colonies were counted after incubation at 37 °C for 24 h.

Subcellular Localization and Lysosomal Acidification assays. Macrophages were stained with Lysotracker Red for 30 min, infected with *E. coli*-eGFP (MOI = 50) for 1 h, and then washed with PBS three times. Alternatively, they were stained with pHrodo-labeled *E. coli* for 1 h. The cells were imaged with laser scanning confocal microscopy.

For subcellular fractionation, the cytosolic and nuclear fractions were separated using a Nuclear and Cytoplasmic Protein Extraction Kit (Beyotime Biotech.). Briefly, one million cells seeded in 60 mm dishes for 24 h were rinsed twice with ice-cold PBS, immediately incubated with cytoplasmic extraction buffer on ice for 15 min, and then harvested using a cell scraper. The samples were vortexed for 30 s, followed by centrifugation at 12,000× g for 10 min at 4 °C, and the supernatant containing cytosolic fraction was transferred to a new tube. The pellet was resuspended in a nuclear extraction buffer on ice for 30 min, followed by centrifugation at 16,000× g for 10 min at 4 °C. The resulting supernatant was collected as the nuclear fraction.

For the lysosomal acidification assay, macrophages were stained with Lysotracker for 1 h or pHrodo-labeled *E. coli* for 1 h, and the cells were imaged with a laser scanning confocal microscope.

Determination of Lactate Concentration. Lactate concentration was measured using a lactate assay kit (Nanjing Jiancheng Bioengineering Institute, Nanjing, China) according to the manufacturer's instructions.

Statistics. Data were presented as the mean value ± SD from the mean. All the experiments were repeated more than three times independently. Student's *t* test or one-way ANOVA was performed using GraphPad Prism 8. Significance was considered at $P < 0.05$.

Data, Materials, and Software Availability. The RNA-seq data were cited from the Gene Expression Omnibus database under accession codes GSE9452 and GSE1710 (64, 65). Other study data are included in the article and/or *SI Appendix*.

ACKNOWLEDGMENTS. We thank Dr. Yayi Hou for providing the pHrodo reagents and Dr. Minsheng Zhu for providing microscope access for imaging. This work was supported by the National Natural Science Foundation of China (#32271221 to K.L., #82170592 to Z.F.), the China Postdoctoral Science Foundation (#2023TQ0154 and #2023M741647 to Z.F.), and the Postgraduate Research Innovation Program of Jiangsu Province (#KYCX22_0182 to C.C.).

Author affiliations: [a]State Key Laboratory of Pharmaceutical Biotechnology, Jiangsu Key Laboratory of Molecular Medicine, Medical School, Nanjing University, Nanjing 210093, People's Republic of China; [b]Department of Vascular Surgery, Nanjing Drum Tower Hospital, Affiliated Hospital of Medical School, Nanjing University, Nanjing 210093, People's Republic of China; [c]Department of General Surgery, Jinling Hospital, Affiliated Hospital of Medical School, Nanjing University, Nanjing 210093, People's Republic of China; [d]Faculty of Biotechnology and Food Engineering, Technion Israel Institute of Technology, Haifa 32000, Israel; [e]Department of Physiology, Biophysics and Neuroscience, Cinvestav, Mexico 07360, Mexico; and [f]Department of Pathology, Nanjing Drum Tower Hospital, Affiliated Hospital of Medical School, Nanjing University, Nanjing 210093, People's Republic of China

1. J. Cui, Y. Liu, J. Li, The new changes of epidemiology, etiology, and clinical characteristics of pyogenic liver abscesses: A retrospective study in a hospital in Northern China. *Infect. Drug Resist.* **16**, 4013–4023 (2023).
2. Y. Chen, Y. Gong, B. Song, Y. Du, K. Cai, Pyogenic liver abscess complicated with endogenous endophthalmitis caused by Klebsiella pneumoniae: A case report and literature review. *Immun. Inflamm. Dis.* **11**, e943 (2023).
3. J. Li *et al.*, Development and validation of a nomogram for predicting sepsis in patients with pyogenic liver abscess. *Sci. Rep.* **13**, 10849 (2023).
4. A. Bläckberg *et al.*, A population-based study of unfavorable prognostic factors associated with pyogenic liver abscess. *Open Forum Infect. Dis.* **10**, ofad352 (2023).
5. J. N. Lin *et al.*, Pyogenic liver abscess in patients with inflammatory bowel disease: A nationwide cohort study. *Liver Int.* **36**, 136–144 (2016).
6. V. Kesar, A. Swaminath, Hepatic masses in a patient with inflammatory bowel disease. *Gastroenterology* **154**, E5–E6 (2018).
7. D. F. Castillo, R. Caicedo, V. Gopalareddy, Liver abscess in a pediatric patient with ulcerative colitis: A case presentation. *J. Clin. Transl. Hepatol.* **7**, 1–4 (2019).
8. A. Bertocchi *et al.*, Gut vascular barrier impairment leads to intestinal bacteria dissemination and colorectal cancer metastasis to liver. *Cancer Cell* **39**, 708–724.e11 (2021).
9. A. Verdugo-Meza, J. Ye, H. Dadlani, S. Ghosh, D. L. Gibson, Connecting the dots between inflammatory bowel disease and metabolic syndrome: A focus on gut-derived metabolites. *Nutrients* **12**, 1434 (2020).
10. Y. Zheng *et al.*, Gut microbiota contributes to host defense against klebsiella pneumoniae-induced liver abscess. *J. Inflamm. Res.* **14**, 5215–5225 (2021).
11. S. W. Jeong *et al.*, Cryptogenic pyogenic liver abscess as the herald of colon cancer. *J. Gastroenterol. Hepatol.* **27**, 248–255 (2012).
12. L. M. Hegarty, G.-R. Jones, C. C. Bain, Macrophages in intestinal homeostasis and inflammatory bowel disease. *Nat. Rev. Gastroenterol. Hepatol.* **20**, 538–553 (2023).
13. S. Van der Merwe, S. Chokshi, C. Bernsmeier, A. Albillos, The multifactorial mechanisms of bacterial infection in decompensated cirrhosis. *J. Hepatol.* **75**, S82–S100 (2021).
14. G. W. Sewell, D. J. B. Marks, A. W. Segal, The immunopathogenesis of Crohn's disease: A three-stage model. *Curr. Opin. Immunol.* **21**, 506–513 (2009).
15. M. Nairz *et al.*, Iron regulatory proteins mediate host resistance to salmonella infection. *Cell Host Microbe* **18**, 254–261 (2015).
16. M. Bonadonna *et al.*, Iron regulatory protein (IRP)-mediated iron homeostasis is critical for neutrophil development and differentiation in the bone marrow. *Sci. Adv.* **8**, eabq4469 (2022).
17. T. A. Rouault, The role of iron regulatory proteins in mammalian iron homeostasis and disease. *Nat. Chem. Biol.* **2**, 406–414 (2006).
18. B. Galy, M. Conrad, M. Muckenthaler, Mechanisms controlling cellular and systemic iron homeostasis. *Nat. Rev. Mol. Cell Biol.* **25**, 133–155 (2023), 10.1038/s41580-023-00648-1.
19. E. G. Meyron-Holtz *et al.*, Genetic ablations of iron regulatory proteins 1 and 2 reveal why iron regulatory protein 2 dominates iron homeostasis. *EMBO J.* **23**, 386–395 (2004).
20. H. Li *et al.*, Iron regulatory protein 2 modulates the switch from aerobic glycolysis to oxidative phosphorylation in mouse embryonic fibroblasts. *Proc. Natl. Acad. Sci. U.S.A.* **116**, 9871–9876 (2019).
21. P. Adamkova *et al.*, Dextran sulphate sodium acute colitis rat model: A suitable tool for advancing our understanding of immune and microbial mechanisms in the pathogenesis of inflammatory bowel disease. *Vet. Sci.* **9**, 238 (2022).
22. C. C. Bain, A. Schridde, Origin, differentiation, and function of intestinal macrophages. *Front. Immunol.* **9**, 2733 (2018).
23. G. Weiss, U. E. Schaible, Macrophage defense mechanisms against intracellular bacteria. *Immunol. Rev.* **264**, 182–203 (2015).
24. M. T. Silva, M. Correia-Neves, Neutrophils and macrophages: The main partners of phagocyte cell systems. *Front. Immunol.* **3**, 174 (2012).
25. C. Yang, X. Wang, Lysosome biogenesis: Regulation and functions. *J. Cell Biol.* **220**, e202102001(2021).
26. Y. B. Hu, E. B. Dammer, R. J. Ren, G. Wang, The endosomal-lysosomal system: From acidification and cargo sorting to neurodegeneration. *Transl. Neurodegener.* **4**, 18 (2015).
27. D. Ploper, E. M. De Robertis, The MITF family of transcription factors: Role in endolysosomal biogenesis, Wnt signaling, and oncogenesis. *Pharmacol. Res.* **99**, 36–43 (2015).
28. Y. Liu *et al.*, Stimulation of hepatic ferritinophagy mitigates Irp2 depletion-induced anemia. *Antioxidants (Basel)* **12**, 566 (2023).
29. J. Shen *et al.*, Protective effects of Hif2 inhibitor PT-2385 on a neurological disorder induced by deficiency of Irp2. *Front. Neurosci.* **15**, 715222 (2021).
30. N. Liu *et al.*, Lactate inhibits ATP6V0d2 expression in tumor-associated macrophages to promote HIF-2α–mediated tumor progression. *J. Clin. Invest.* **129**, 631–646 (2019).
31. Anonymous, Manuscript descriptor form. *Clin. Gastroenterol. Hepatol.* **3**, A20 (2005).
32. M. Margalit, H. Elinav, Y. Ilan, M. Shalit, Liver abscess in inflammatory bowel disease: Report of two cases and review of the literature. *J. Gastroenterol. Hepatol.* **19**, 1338–1342 (2004).
33. J. Song *et al.*, Liver abscess and diarrhea as initial manifestations of ulcerative colitis: Case report and review of the literature. *Digest. Dis. Sci.* **48**, 417–421 (2003).
34. P. D. Smith *et al.*, Intestinal macrophages and response to microbial encroachment. *Mucosal Immunol.* **4**, 31–42 (2011).
35. K. De Muynck, B. Vanderborght, H. Van Vlierberghe, L. Devisscher, The gut-liver axis in chronic liver disease: A macrophage perspective. *Cells* **10**, 2959 (2021).
36. O. Krenkel, F. Tacke, Liver macrophages in tissue homeostasis and disease. *Nat. Rev. Immunol.* **17**, 306–321 (2017).
37. E. Barreby, P. Chen, M. Aouadi, Macrophage functional diversity in NAFLD–More than inflammation. *Nat. Rev. Endocrinol.* **18**, 461–472 (2022).
38. S. Tran *et al.*, Impaired kupffer cell self-renewal alters the liver response to lipid overload during non-alcoholic steatohepatitis. *Immunity* **53**, 627–640.e625 (2020).
39. D. Ferring-Appel, M. W. Hentze, B. Galy, Cell-autonomous and systemic context-dependent functions of iron regulatory protein 2 in mammalian iron metabolism. *Blood* **113**, 679–687 (2009).
40. C. Chelakkot, J. Ghim, S. H. Ryu, Mechanisms regulating intestinal barrier integrity and its pathological implications. *Exp. Mol. Med.* **50**, 1–9 (2018).
41. A. Larabi, N. Barnich, H. T. T. Nguyen, New insights into the interplay between autophagy, gut microbiota and inflammatory responses in IBD. *Autophagy* **16**, 38–51 (2019).
42. S. R. Bonam, F. Wang, S. Muller, Lysosomes as a therapeutic target. *Nat. Rev. Drug Discov.* **18**, 923–948 (2019).
43. C. Settembre *et al.*, TFEB links autophagy to lysosomal biogenesis. *Science* **332**, 1429–1433 (2011).
44. G. Napolitano, A. Ballabio, TFEB at a glance. *J. Cell Sci.* **129**, 2475–2481 (2016).
45. M. Abdulla, N. Mohammed, A review on inflammatory bowel diseases: Recent molecular pathophysiology advances. *Biol. Targets Ther.* **16**, 129–140 (2022).
46. K. F. Yambire *et al.*, Impaired lysosomal acidification triggers iron deficiency and inflammation in vivo. *Elife* **8**, e51031 (2019).
47. R. A. Weber *et al.*, Maintaining iron homeostasis is the key role of lysosomal acidity for cell proliferation. *Mol. Cell* **77**, 645–655.e7 (2020).
48. J. K. Byun *et al.*, Oncogenic KRAS signaling activates mTORC1 through COUP-TFII–mediated lactate production. *EMBO Rep.* **20**, e47451 (2019).
49. J. A. Martina, Y. Chen, M. Gucek, R. Puertollano, MTORC1 functions as a transcriptional regulator of autophagy by preventing nuclear transport of TFEB. *Autophagy* **8**, 903–914 (2012).
50. Z. Cui *et al.*, Structure of the lysosomal mTORC1-TFEB-Rag-Ragulator megacomplex. *Nature* **614**, 572–579 (2023).
51. Y. J. Song *et al.*, Inhibition of lactate dehydrogenase A suppresses inflammatory response in RAW 264.7 macrophages. *Mol. Med. Rep.* **19**, 629–637 (2019).
52. M. C. Ghosh *et al.*, Therapeutic inhibition of Hif-2α reverses polycythemia and pulmonary hypertension in murine models of human diseases. *Blood* **137**, 2509–2519 (2021).
53. S. A. Anderson *et al.*, The IRP1-HIF-2α axis coordinates iron and oxygen sensing with erythropoiesis and iron absorption. *Cell Metabol.* **17**, 282–290 (2013).
54. M. Sanchez, B. Galy, M. U. Muckenthaler, M. W. Hentze, Iron-regulatory proteins limit hypoxia-inducible factor-2α expression in iron deficiency. *Nat. Struct. Mol. Biol.* **14**, 420–426 (2007).
55. M. Ghabril *et al.*, Liver injury from tumor necrosis factor-α antagonists: Analysis of thirty-four cases. *Clin. Gastroenterol. Hepatol.* **11**, 558–564.e3 (2013).
56. H. S. Ban, Y. Uto, H. Nakamura, Hypoxia-inducible factor (HIF) inhibitors: A patent survey (2016–2020). *Expert Opin. Ther. Pat.* **31**, 387–397 (2021).
57. S. S. Cooperman *et al.*, Microcytic anemia, erythropoietic protoporphyria, and neurodegeneration in mice with targeted deletion of iron-regulatory protein 2. *Blood* **106**, 1084–1091 (2005).
58. T. LaVaute *et al.*, Targeted deletion of the gene encoding iron regulatory protein-2 causes misregulation of iron metabolism and neurodegenerative disease in mice. *Nat. Genet.* **27**, 209–214 (2001).
59. S. Y. Jeong *et al.*, Iron insufficiency compromises motor neurons and their mitochondrial function in Irp2-null mice. *PLoS One* **6**, e25404 (2011).
60. H. Li *et al.*, Iron regulatory protein deficiency compromises mitochondrial function in murine embryonic fibroblasts. *Sci. Rep.* **8**, 5118 (2018).
61. J. S. Shapiro *et al.*, Iron drives anabolic metabolism through active histone demethylation and mTORC1. *Nat. Cell Biol.* **25**, 1478–1494 (2023).
62. T. Xu *et al.*, Hormone replacement therapy for postmenopausal atherosclerosis is offset by late age iron deposition. *Elife* **12**, e80494 (2023).
63. R. Boxio, C. Bossenmeyer-Pourié, N. Steinckwich, C. Dournon, O. Nüsse, Mouse bone marrow contains large numbers of functionally competent neutrophils. *J. Leukoc. Biol.* **75**, 604–611 (2004).
64. J. Olsen *et al.*, Definition of an ulcerative colitis preinflammatory state. Gene Expression Omnibus. https://www.ncbi.nlm.nih.gov/geo/query/acc.cgi?acc=GSE9452. Deposited 29 October 2007.
65. C. M. Costello *et al.*, Expression profiling in inflammatory bowel disease. Gene Expression Omnibus. https://www.ncbi.nlm.nih.gov/geo/query/acc.cgi?acc=GSE1710. Deposited 27 August 2004.